HI Observation and Detection Near Galactic Anti-Center

Max Lee *

Lab Partners: Basil Kyriacou, Connor McWard , James Mang

Department of Astronomy, University of California, Berkeley

Abstract

The 21 cm hyper-fine hydrogen emission (HI) has historically been used to calculate the rotation curve and structure of the milky way through velocity analysis of hydrogen clouds. Here we continue this work and provide evidence of HI emission near the galactic anti-center in the plane of the milky way at $l = 120°$, $b = 0°$, and deduce characteristic properties of the evident neutral hydrogen clouds. We find that 2 significant clouds of neutral hydrogen in our line of sight appear to move away from each other with velocities of $\sim 38\,km\,s^{-1}$ and $\sim -2\,km\,s^{-1}$ relative to our local standard of rest. Further we find that the absolute temperatures of the clouds far exceed our expectations and are measured to be at $\sim 143\,K$ and $\sim 5092\,K$. We show that these anomalous temperatures, along with rotational velocity calculations provide evidence for the differential rotation of gas clouds in the Milky Way.

1 Introduction

The 21-cm Hydrogen line (HI) is the result of neutral hydrogen's hyper-fine energy transition, where the spin alignment of the electron and proton go from aligned to anti-aligned. This energy difference is small and rare, but the emission wavelength is predictable and detectable with radio telescopes. More over, the abundance of neutral hydrogen throughout the universe makes HI a useful probe for conducting science in a variety of fields.

In recent years, radio telescopes such as the *Hydrogen Epoch of Reionization Array* (HERA) have been working to detect the Hydrogen 21cm line from the Epoch of reionization to better understand the formation of the first energy sources in the universe [DeBoer et al., 2017]. Similarly, works by Mitchell et al. [2018] have used it to determine galaxy structure and evolution in a cosmological context and Koo et al. [2017] to understand spiral structures in our own galaxy.

Here we show evidence of the HI line in the Milky way galaxy and use this to extrapolate radial and rotational velocities of neutral hydrogen clouds as well as their associated brightness temperatures and thermal properties. We begin with a review of the HI emission, temperature definitions and astrophysical coordinate transformations in section 1.1. This is followed by a detailed description of our instrumentation techniques in section 2. We present our experimental results of the HI line and its intensity in section 3, which we use to extrapolate characteristic

temperatures, distances and velocities in section 4. We conclude by recapping our observations and posing questions for future work in section 5.

1.1 Background

For a neutral hydrogen atom, the proton and electron (both fermions) contain magnetic dipole moments that can be either aligned or anti-aligned. The magnetic moments when aligned have less energy because there exists a finite probability that the proton and electron become super imposed and their magnetic moments cancel out. This means when the magnetic moments are anti-aligned, the neutral hydrogen atom will spontaneously change to its lower energy state releasing a wavelength proportional to its energy change at $21\,cm$ or $1.402\,MHz$ [Furlanetto, 2016].

The Einstein emission coefficient $A_{1,0}$ for this transition can be found with knowledge of neutral hydrogen's magnetic dipole moment in the anti-aligned state and frequency of emission. The inverse of $A_{1,0}$ represents the half life of the transition, and while we defer the reader to more in-depth quantum mechanical treatments and derivations, we provide the half life result here to emphasize the rarity of this transition.

$$A_{1,0}^{-1} = \frac{3hc^3}{64\pi^4 \nu_{21cm}^3 |\mu_{1,0}^*|^2}$$

$$\sim 2.85 \times 10^{15}\, s \sim 9 \times 10^7\, years \tag{1}$$

Where h is Planks constant, c is the speed of light, ν_{21cm} is the frequency of the HI emission - $1420.405751\, MHz$ - and $|\mu_{1,0}^*|$ is the magnitude of the complex conjugate of the mean anti-aligned magnetic dipole moment in the ground state of neutral hydrogen - $9.27 \times 10^{-21}\, erg\, gauss^{-1}$.

This is an incredibly rare signal and would be useless if not for the sheer abundance of neutral hydrogen through out the universe. Still, the signal we receive is weak, and requires accurate instrumentation to see.

Though the signal is weak, it is well within the limit of low frequencies where $h\nu << kT$, thus the Planck Blackbody function can be simplified using the Rayleigh approximation such that,

$$B_\nu = \frac{8\pi h}{c^3} \frac{\nu^3}{e^{h\nu/k_b T} - 1} \sim \frac{2k_b T \nu^2}{c^2} \tag{2}$$

Where B_ν is intensity, k_b is Boltzmann's constant, h is Planks constant, T is the temperature of the source ν is the frequency and c the speed of light. Eq 2 implies that the intensity is directly proportional to the temperature. More generally, using eq 2, the intensities of any noise source - such as the HI signal - at a given frequency can be described in terms of its *Brightness Temperature* T_B, which is the temperature a source would be if it were a blackbody. We compute the intensity I_ν by sampling time series voltage data, $V(t)$, and computing the power spectrum which we define as,

$$P(\nu) = |F(V(t))|^2 \tag{3}$$

Rewriting equation (2) for brightness temperature we have,

$$T_B = \frac{I_\nu c^2}{2k_b \nu^2} \tag{4}$$

Brightness temperature provides a physical comparison of intensity supplied by the system receiving, T_{rx}, and sky, T_{sky}, in the same units. The system temperature represents the sum of both of these contributions i.e. $T_{sys} = T_{rx} + T_{sky}$ and allows us to analyze our results in meaningful units that correspond to physical quantities. Further, this makes calibrating our signal easier because we can reference our measurements to known temperatures of noise sources.

The question of when and where to point the antenna depends on coordinate choice, time and their respective definitions. To account for the motion of
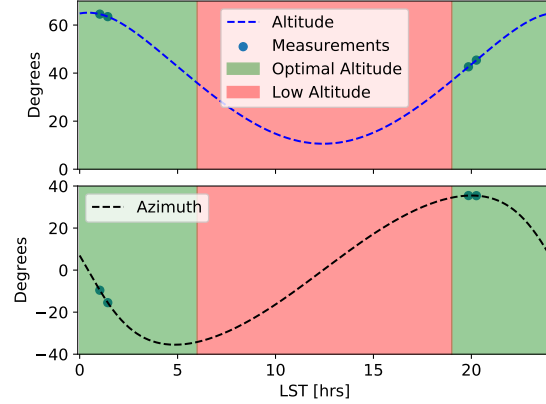

Figure 1: We observe near the galactic anti-center ($l = 120°, b = 0°$), 4 times over the course of two days, at the times altitudes and azimuths represented by the scatter points shown in blue. To ensure the best possible data, we only taking data when our source is above $36°$ altitude represented in the green portions.

distant stars with respect to earths reference frame we use sidereal time, a measure of our rotation relative to our axis and centered at the vernal equinox. We shift sidereal time to our longitude and use Local Sidereal Time (LST), which ensures that stars are at our zenith at a LST equal to their right ascension (discussed below). We obtain the current local sidereal time (LST) using *ugradio.timing*[1] package which provides the current LST in radians.

Pointing the telescope requires us to consider coordinate systems and positional definitions of sources. We use Topocentric, Equitorial, and Galactic coordinates which describe: the angle from north and altitude above the horizon at an earth location, the projected longitude (right ascension, α) and latitude (declination δ) into the universe, and the angle around and above the milky way respectively. In this work we focus our attention to galactic coordinates (galactic longitude) $l = 120\,$deg, (galactic latitude) $b = 0\,$deg and we convert this location to Topocentric coordinates in earths reference frame for accurate telescope pointing, and Equitorial coordinates for Local Standard of Rest velocity corrections (See Appendix B for coordinate conversions).

---

[1]https://github.com/AaronParsons/ugradio

2   Instrumentation

Our antenna is a pyramid shaped horn of receiving area $\sim 0.28\,m^2$ and base length of $\sim 54\,cm$ located at UC Berkeley's Radio Observatory ($lat = 37.87°$, $lon = -122.25°$, $alt = 120°$). Because of the relatively small receiving aperture, the angular resolution of the telescope, described by,

$$\theta \sim \lambda/D \tag{5}$$

is $\sim 35°$. While this prevents pointing accuracy, it also allows for longer integration times without having to manually move the telescope.

We use a signal chain that first receives the signal in an impedance matching circuit containing an antenna, balan and resistor. Because of the importance of transmission lines and impedance we discuss this further in Appendix A. The signal is then filtered and mixed through a Double Heterodyne Mixer, the first component of which is a double side-band mixer (DSB), with a local oscillator (LO) at $1230\,MHz$. Further filtering happens through a ?????? MHz Band-pass removing high and low frequency components centered at $\sim 190\,MHz \pm 30\,MHz$. This then enters the second component of the Double Heterodyne Mixer, a single side-band mixer (SSB) to further down mix the frequency. For the SSB, we use an LO of $190\,MHz$ and a $95°$ phase shift followed by a $2\,MHz$ filter creating a base-band of $\pm 2\,MHz$ centered at $0.4\,MHz$.

We note interference in our signals at frequencies of $106.9\,MHz$ and $94.1\,MHz$ from local radio stations after mixing. Because of this we sample at $62.5\,MHz$ which causes the interference to alias to $9\,MHz$ and $15\,MHz$ respectively, which is well outside of our final $2\,MHz$ filter.

Obtaining the hydrogen line involves measurements to observe the shape and measurements of the intensity. For the prior we use in-band frequency switching, the process of adjusting the LO of the DSB so that the HI signal appears in independent side-bands. We sample for two long integration's (s_{on}, s_{off}), which captures the filter shapes in each so that it can be removed by dividing the two and leaving only the HI line, $s_{line} = s_{on}/s_{off}$. Alternatively, we could have used out of band frequency switching with an LO set such that the HI signal was out of the $2\,MHz$ bandwidth, but this method lacks the extra observation of H1 we recieve in in-band frequency switching.

To accomplish in-band frequency switching, we set the LO for the DSB of $1231\,MHz$ for the s_{on} measurements and $1229\,MHz$ for s_{off}. This results in a peak at intermediate frequency (IF) of $1.4\,MHz$ for s_{line}.

Observing the intensity of the signal requires we find the temperature of the system, including the temperatures of the receiver, antenna and hydrogen. Knowledge of the system temperature and quick measurements of the intensity both on and off the line, allow us to convert our measured intensities to units of temperature. We calculate this *gain* with a short integration of the cold sky (s_{cold}) and short integration of a known noise source (s_{cal}), humans, which radiate with $T_b = 300\,K$. Because the sky temperature is much smaller than our calibration temperature we neglect it and calculate the gain, G, as,

$$G = \frac{T_{cal}}{\sum s_{cal} - s_{cold}} \sum s_{cold} \tag{6}$$

With the gain, we can convert our line shape into units of temperature by multiplying so that,

$$T_{line} = G \times s_{line} \tag{7}$$

3   Results

We obtain the line shape by digitally sampling at $62.5\,MHz$ in 100 block intervals of 20^5 samples per block. We perform this over 400 iterations providing us with 8×10^9 samples, half of which are real and half imaginary components of the SSB. We perform this both on and off the line and median over power spectra for each block of data culminating in s_{line} through division. We further convolve over frequency channels using *scipy.signal.savgol-filter* with a window size of 51 and polynomial degree of 7.

Our observations involve two consecutive viewings on JD 2458906, and two more on 2458907 (see figure 1). On JD 2458906, our integration time is 18 minutes beginning at 1.02 hrs LST and ending at 1.63 hrs LST after the second integration. The following day, JD 2458907, we observe for 40 minutes, again with two consecutive viewings, beginning at 19.85 hrs LST, ending on 20.25 hrs LST. We expect the hydrogen line to exist at $0.4\,MHz$ in the base band, which after correcting for the adjusted LO's should have a zero offset. We see in fig 2 that our observations show it to be at $0.15 \pm 0.35\,MHz$, which shows a small offset of 0.15.

We calibrate with two short integration's, one on coordinates $l = 120°, b = 0°$ and one with the aperture blocked by humans providing noise at $T = 300\,K$. Using equation 6, we find the gain to be

Avg [MHz]	Avg Doppler [km/s]	Avg LSR Corrected [km/s]	Amplitude [K]	σ [MHz]	σ [km/s]
-0.0188	25.1	38.64	45.88	0.0468	15.4227
0.179	-16.2	-2.68	25.23	0.0911	24.77

Table 1: We fit Gaussian's to our HI emissions in base band, as a function of velocity and with corrected LSR velocity. We find that there are two distinct Gaussian's which fit with the data and indicate that there are two clouds of neutral hydrogen in our line of sight. Further we find that the red-shifted cloud is almost twice as bright as the blue shifted cloud.
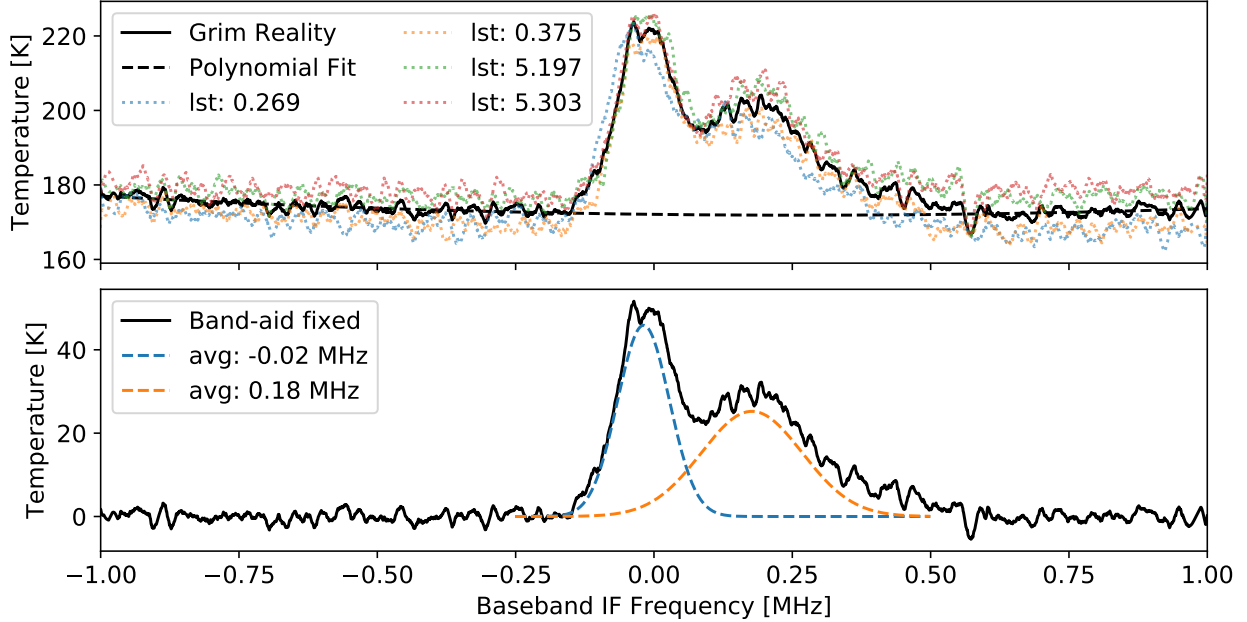

Figure 2: We show the averaging of 4 separate observations (*dotted lines*) and the 'Naively' calculated system temperature (*grim reality*). The first amplifier shape and noise contribution are subtracted from our HI signal by fitting a first degree polynomial (*Black Dashed*). This removes the additional spectral structure and power leaving us with power representing solely the HI line (*band aid fixed*). Using this we fit two Gaussian's to the data and find a broad and cold blue shifted Gaussian for one, and a narrow, bright and red shifted Gaussian for another.

$G = 180.45$. We scale our s_{line} measurements using this, and see in the top panel of figure 2 that the HI line rests on a sloped line sitting at $\sim 175\,K$ which is caused by the noisy first amplifier of the Big Horn. To remove this boost We fit a polynomial modelling the first amplifiers gain contribution which can be subtracted from our results. This has the effect of scaling noise un-related to the HI line to $0K$, removing the spectral structure of the first amplifier and making our only temperature contribution come from HI line emissions.

After removing the shape of the first amplifier, we fit Gaussian's to the peaks of our data, and we find 2 primary Gaussian's with amplitudes, averages and standard deviations seen in table 1. It is useful to convert the frequency axis to velocity, as we will use

it in section 4 various calculations. To do this, We first moved our base-band frequency data to RF frequency by adding the components of the LO's across our double heterodyne mixer. We then use these frequency's to calculate the approximated Doppler shift,

$$\frac{v}{c} = \frac{\Delta\nu}{\nu_0} \qquad (8)$$

Where $\Delta\nu$ is the difference from the expected 21cm Emission at $\nu_0 = 1420.4\,MHz$ and c is the speed of light. Because the earth is orbiting around its axis, the sun, and the galaxy, we further correct the velocities by calculating the Local Standard of Rest frame correction, using *ugradio.doppler.get projected velocity*. This requires the right ascension and declination of $l = 120, b = 0$ which we find using the rotation matrix detailed in Appendix B. We find a correction

of $V_{correction} = -13.54\,km/s$ represented by the arrows in figure 3. This transformation is linear and allows us to further adjust the values of the averages and sigmas for the fitted Gaussian's so that they are functions of velocity as well (see table 1).

4   Interpretation

Figures 2 and 3, and table 1 provide us with a plethora of information about our observations. They first detail the brightness temperature and therefore intensity of the H1 line seen in each Gaussian. Further they provide velocity information specific to the individual peaks implying separate properties and multiple clouds of neutral hydrogen. Here we check that our velocity measurements are reasonable by comparing with an estimate of the escape velocity of the milky way, then calculate the thermal temperatures of the gas clouds using the standard deviations of our gaussian fits. With this we discuss the possibility of a spiral structure in our milky way and evidence of differential rotation.

Before continuing we provide a quick sanity check of our results with a rough estimation of the escape velocity of the Milky Way and compare with our final LSR velocities. Most recent estimates place the mass of the Milky Way galaxy at $10^{12}\,M_\odot$ Wang et al. [2019], with a radius that we set to $\sim 50\,kpc$ following Taylor et al. [2016]. We ignore the density distribution and treat the milky way as simply a point mass to get a feel of what the escape velocity would be in this scenario

$$\frac{1}{2}mv_{esc}^2 = \frac{GM_{mw}m}{R_{mw}}$$
$$v_{esc} = \sqrt{\frac{2GM_{mw}}{R_{mw}}} \qquad (9)$$
$$v_{esc} = 414.77 km/s$$

This is a lower limit on the escape velocity which for our purposes is good enough to show that our maximum velocity $(-80km/s)$ is well within a reasonable range to be bound to the Milky Way[2].

The temperatures that we measure at the peaks of our two Gaussian's (1) show two distinct averages, brightness temperatures and standard deviations. We take this to be evidence of two clouds of hydrogen that we are observing in the same line of sight, but moving in different directions relative to us. With this and our measurements of average velocities and standard deviations, we can find evidence for the spiral structure.

The velocities seen in figure 3, are representative of the spread in individual hydrogen atoms moving in the cloud with the average velocity being the radial component of the clouds motion. Notice that the spectra have 'flipped' when compared to the base band IF axis in figure 2. This is because the hydrogen observed at greater than $0\,MHz$ have more energy, and are blue-shifted, moving towards us with a negative velocity, while the observations at less than $0\,MHz$ have less energy and are therefore red-shifted, moving away with a positive velocity.

By considering the standard deviation of the velocity distributions (σ in table 1), which are related to the rms velocity of the particles in the HI cloud, and assuming an ideal gas we can say that the root mean square velocity of a hydrogen particle is,

$$v_{rms} = \sqrt{\frac{3k_b T}{m}}. \qquad (10)$$

Where T is the thermal temperature of particles, m is the mass of a neutral hydrogen atom and v_{rms} is equal to the standard deviation σ. Solving this for the thermal temperature we find the clouds to be at, $143\,K$ and $5092\,K$ for the bright red-shifted cloud and dim blue-shifted cloud respectively.

We can further investigate table 1 and figure 3 by calculating the angular velocity of the clouds. If we assume that the motion of the milky was is rigid, then all of the angular velocities should be the same. Under the assumption that the sun is traveling at a constant tangential velocity $V_0 = 220 \pm 10\,km\,s^{-1}$ at a radius of $8 \pm .5\,kpc$ from the galactic center. Assuming rigid body motion of the suns rotation, $\omega_0 = V_0/R_0 \sim 29 \pm 1\,km\,s^{-1}\,kpc^{-1}$.

Based off of the geometry of the problem, we can find the angular velocity of the hydrogen clouds with,

$$\omega_{HI} = \frac{V_r}{R_0 \sin(l)} + \omega_0 \qquad (11)$$

which leads to angular velocities of $\omega_{blue} = 28.56\,km\,s^{-1}\,kpc^{-1}$, $\omega_{red} = 21.69\,km\,s^{-1}\,kpc^{-1}$ for the blue shifted and red shifted clouds respectively, highlighting that they are not in fact the same and seem to have some radial dependence.

Considering the broadening of the blue-shifted HI cloud, our thermal calculations aligns with what we would theoretically predict, that there is a higher temperature, causing more thermal motion and a broader spread in velocities. What does not align with theory is that these temperatures are high compared to what we would estimate. In the cold interstellar medium, neutral hydrogen clouds generally exist at $\sim 100\,K$. The existence of temperature an

---

[2]The most recent calculation of the Milky Way escape velocity places it at $544^{+64}_{-46}\,km/s$ [Wang et al., 2019]
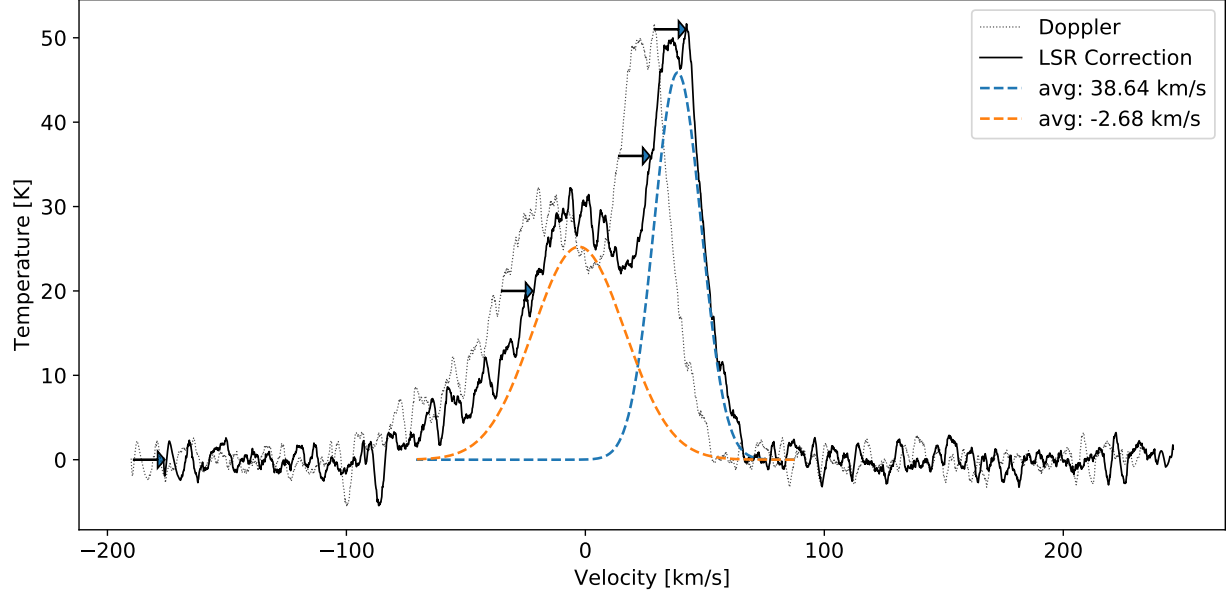
Figure 3: After calculating the Doppler shifted velocity of our HI measurements, (*black dotted*), we correct it for the Local standard of rest frame, which has the effect of red shifting our velocities (*black solid*). Because the transformation from frequency to velocity is linear, we are able to easily convert the Gaussian's in fig 2 to functions of velocity in the corrected frame. We note that the two Gaussian's are representative of two HI clouds at different distances and brighnesses along our line of sight.

order of magnitude larger than this implies structures in the clouds imposing a broadening to v_{rms}.

Further, the angular velocities imply that the blue shifted cloud is orbiting at a greater angular velocity when compared to the red-shifted cloud. For rigid body rotation, we would assume that the angular velocity at all points in the disk have the same frequency. The fact that this is not the case implies that a different form of rotation is occurring.

We believe that sources with this high of a temperature difference, and non-aligned angular velocity imply evidence of differential rotation in the HI clouds we are observing, meaning particles are rotating with a angular velocity proportional to $1/R$ where R is the distance of the object from the galactic center, and the tangential velocity of all objects is constant. If we consider this to be the case, we can make the argument that the blue shifted cloud, which is rotating faster, is actually much closer to us than the red shifted cloud.

Further if we extrapolate this out to the rest of the Milky Way, it seems that the rotation of the galaxy as a whole is not rigid, but differential implying there is a constant rotational velocity in the Milky Way. This would be evidence that our observations are of spiral arm structures in the galaxy.

5 Conclusion

In this work we provided experimental evidence of HI emissions in the Milky Way Galaxy by observing frequencies of $1420.4 \pm 2 \, MHz$, the expected emission wavelength of the HI transition. We provide an overview of the HI emission in section 1, followed by a detailed description of our instrumentation and calibration methods in section 2. We then highlight the results of our experimentation in section 3 where we show our measurements of the brightness temperature of what we believe are two neutral hydrogen clouds along our line of sight. Further we provide estimates of the velocities of the clouds from a Doppler shifted perspective as well as a LSR corrected frame. We use these observations to motivate a study of rotational velocities and thermal properties of the clouds, and their relation to the possible differential rotation of the Milky Way in section 4.

This experiment leaves us with many questions about the structure of our galaxy and events happening in gas clouds. What is causing the large temperatures we find in these HI clouds? Why are the temperatures between the two clouds so different? How fast are the clouds moving tangentially to our position? Can we find a distance to the sources? How many other clouds are out there? What is the nature

of the differential rotation of the HI clouds we are observing?

While we were viewing the HI line at one galactic latitude and longitude, we believe a more in depth study spanning the full range of galactic longitudes, with distance estimates, could hold the answers to the frontiers of our knowledge.

6   Acknowledgments

References

David R. DeBoer, Aaron R. Parsons, James E. Aguirre, Paul Alexander, Zaki S. Ali, Adam P. Beardsley, Gianni Bernardi, Judd D. Bowman, Richard F. Bradley, Chris L. Carilli, Carina Cheng, Eloy de Lera Acedo, Joshua S. Dillon, Aaron Ewall-Wice, Gcobisa Fadana, Nicolas Fagnoni, Randall Fritz, Steve R. Furlanetto, Brian Glendenning, Bradley Greig, Jasper Grobbelaar, Bryna J. Hazelton, Jacqueline N. Hewitt, Jack Hickish, Daniel C. Jacobs, Austin Julius, MacCalvin Kariseb, Saul A. Kohn, Telalo Lekalake, Adrian Liu, Anita Loots, David MacMahon, Lourence Malan, Cresshim Malgas, Matthys Maree, Zachary Martinot, Nathan Mathison, Eunice Matsetela, Andrei Mesinger, Miguel F. Morales, Abraham R. Neben, Nipanjana Patra, Samantha Pieterse, Jonathan C. Pober, Nima Razavi-Ghods, Jon Ringuette, James Robnett, Kathryn Rosie, Raddwine Sell, Craig Smith, Angelo Syce, Max Tegmark, Nithyanandan Thyagarajan, Peter K. G. Williams, and Haoxuan Zheng. Hydrogen Epoch of Reionization Array (HERA). , 129(974):045001, April 2017. doi: 10.1088/1538-3873/129/974/045001.

Carl J. Mitchell, J. A. Sellwood, T. B. Williams, Kristine Spekkens, Rachel Kuzio de Naray, and Alex Bixel. The RINGS Survey. III. Medium-resolution Hα Fabry-Pérot Kinematic Data Set. , 155(3):123, March 2018. doi: 10.3847/1538-3881/aaabb8.

Bon-Chul Koo, Geumsook Park, Woong-Tae Kim, Myung Gyoon Lee, Dana S. Balser, and Trey V. Wenger. Tracing the Spiral Structure of the Outer Milky Way with Dense Atomic Hydrogen Gas. , 129(979):094102, September 2017. doi: 10.1088/1538-3873/aa7c08.

Steven R. Furlanetto. *The 21-cm Line as a Probe of Reionization*, volume 423 of *Astrophysics and Space Science Library*, page 247. 2016. doi: 10.1007/978-3-319-21957-8_9.

Wenting Wang, Jiaxin Han, Marius Cautun, Zhaozhou Li, and Miho N. Ishigaki. The mass of our Milky Way. *arXiv e-prints*, art. arXiv:1912.02599, December 2019.

Corbin Taylor, Michael Boylan-Kolchin, Paul Torrey, Mark Vogelsberger, and Lars Hernquist. The mass profile of the Milky Way to the virial radius from the Illustris simulation. , 461(4):3483–3493, October 2016. doi: 10.1093/mnras/stw1522.

Appendices

A   Wave Guides

The HI line is made up of photons with electric fields traveling through space in a vacuum. It makes its way through a chain of conducting wires where the voltage on those conductors is sampled digitally and we are able to preform the analysis as in section 4. This is an incredibly complicated process and requires at minimum an understanding of the lines used to transmit the signal. Here we provide a brief overview of transmission lines and wave guides, involving an experiment to calculate the speed of light, and geometry of a wave guide. This sheds insight into our receiving system and possible sources of error. We begin with a description of transmission lines and wave guides, followed by experimental results with C-band - $\sim 3\,GHz$ - and X-band - $7-12\,GHz$ - wave guides. We find evidence supporting the current estimation of the speed of light using least squares, and highlight the 2 distinct velocities in a wave guide: the phase and group velocities. Further we show that with knowledge of the frequency and location of the nulls alone, the geometry of the guide can be extrapolated.

A.1   Transmission lines and Wave guides Background

Transmission lines are simply conductors which allow the propagation of an electric signal. In our measurements of the HI line, the transmission lines present are the vacuum of space allowing the electromagnetic waves from the HI emission to propagate and the physical 2 conductor, dielectric filled cables carrying the signal through our signal chain. Transmission

line impedance, or complex resistance, is determined solely by the capacitance per unit length and inductance per unit length according to the relation,

$$Z_{trans} = \sqrt{\frac{L}{C}} \qquad (12)$$

Where Z_{trans} is the complex impedence of the transmission line, L is the inductance per unit length and C is the capacitance per unit length. Equation 12 represents the ratio of the voltage to current at some instant in time and some location in a transmission line for a single traveling wave (cite transline).

When signal transfers from one transmission line to the next, the interaction of their impedance's can cause reflections of signal, signal dispersion and a time delay. Our Big Horn is fixed with a dipole antenna, Balan and resistor circuit upon first contact with the HI signal for the sole purposes of matching the impedance of it traveling through free space and entering $50\,\Omega$ BNC cables. Wave guides are systems controlling the direction of the waves propagation and here we measure the effect of reflection and interference of waves in them.

We use least squares estimations to calculate the speed and phase shift of our signal in the C-band wave guide and more over, find the shape in the X-band wave guide.

A.2 Wavelength Measurements in a Wave Guide

We perform 2 experiments to measure the effect of reflections and interference in the wave guide. One with a long - C-band - slotted coaxial line measuring a $3\,GHz$ input frequency and the second with a short - X-band - slotted coaxial line measuring frequencies from $7.5-11.25\,GHz$ of input frequency in increments of $0.75\,GHz$. For both experiments we measure the nulls of the waves in the wave guide with both open and closed endings representing both high and low impedance matching.

We use least squares estimations which minimizes χ^2 defined as,

$$\frac{\partial \chi^2}{\partial \vec{p}} = \frac{\partial}{\partial \vec{p}} \sum_i \frac{|y_i - f(\vec{x}_i, \vec{p})|^2}{\sigma_i^2} = 0 \qquad (13)$$

Where x_i are our inputs, $\vec{p}$ are parameters of the model, y_i is the expected solution and σ_i is the noise in our model. By using eq 13 we can find the maximum likely hood solution for input parameters.
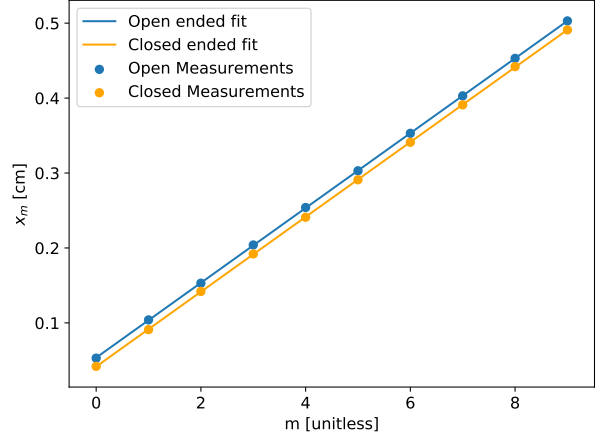

Figure 4: We measure the nulls of a $3\,MHz$ sine wave through a wave guide with both an open and closed end to test low and high impedence reflections. We find that the slope, or wavelength, calculated in a least squares approximation is the same regardless of the impedance, but there is a phase offset such that the line for the closed measurement has a delay of $0.0119\,cm$.

A.3 C-Band Results

We measure the locations of the nulls for a $3\,MHz$ free space frequency and use this data and a least squares estimator to solve for the slotted wave guide wavelength λ_{sl}. We use the equation,

$$x_m = A + m\frac{\lambda_{sl}}{2} \qquad (14)$$

where x_m is the position of the mth null and $lambda_{sl}$ is the wavelength in the slotted waveguide.

Figure 4 shows our results from the C-band measurements and the least squares fitting. We find that when the wave guide ends are both open and closed, the slotted wavelength is the same, but the effect of closing the end of the guide creates a phase difference or delay, to our measurements. The delay is equal to the difference in the constant A in eq 14. We find this to be $0.0199\,cm$. We also calculate the speed of transmission in the wave guide using the calculated wavelength and the input frequency. For both open and closed, the speed is $2.996 \times 10^8\,m\,s^{-1}$.

A.4 X-Band Results

We take measurements of nulls in the X-band wave guide for 6 different free space frequencies. We use these measurements with eq 14 to calculate the guide wavelength, λ_g, with a least squares estimator. We then use the results of this and knowledge of the free

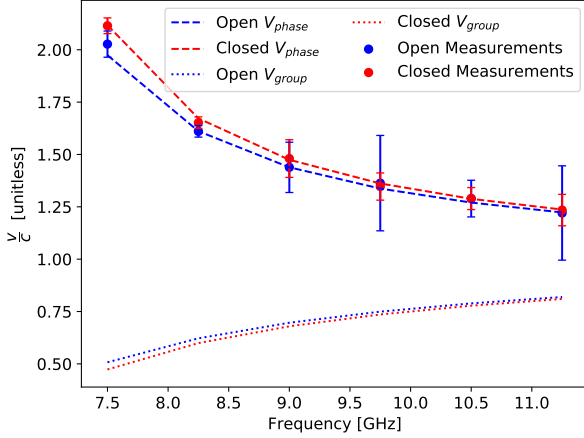Figure 5: We show the phase velocity of both the open ended and closed X-band wave guide for 6 frequencies spanning $7.5 - 11.25\,MHz$. We fit the data using a least squares solution and calculate the phase velocity with equation 15. We normalize the velocity to the speed of light c so that the effect of phase velocity being faster than the speed of light is clear.

space wave lengths, λ_{fs} to perform a least squares estimate on the group wavelength equation given by,

$$\lambda_g = \frac{v_p}{\lambda_{fs}} = \frac{\lambda_{fs}}{[1 - (\lambda_{fs}/2a)^2]^{1/2}} \qquad (15)$$

Where a is the width of the X-band wave guide. We rearrange this so that it can be used in a first degree polynomial fit,

$$\left(\frac{\lambda_{fs}}{\lambda_g}\right)^2 = -\left(\frac{\lambda_{fs}}{2}\right)^2 \cdot \frac{1}{a^2} + 1 \qquad (16)$$

In this formation, we can see that while λ_g depends non linearly on a, we can still use linear polynomial fit to find the least squares solution to the equation by plugging in the previously calculated $(\lambda_{fs}/\lambda_g)^2$ as the y values, $(\lambda_{fs}/2)^2$ as the x values and solving for the slope, $-1/a^2$, and the y-intercept which we expect to be 1 in this case. We find that for open and closed measurements, the width of the wave guide is $2.32\,cm$ and $2.27\,cm$ respectively. As we would expect, the values of the y intercept are 0.99 and 1.003 for open and closed respectively.

Using equation 15, we calculate the phase velocity of our waves with the values of a and λ_g from our polynomial fit, and similarly we calculate the group velocity given by the inverse of equation 15. Figure 5 shows the calculated phase velocity for both the open and closed ended wave guide measurements at the 6 frequencies of experimentation. We normalize the

velocities to the speed of light c to emphasize the fact that the phase velocities appear to be going up to ~ 2 times the speed of light in the wave guide, while the group velocity is always less than c!

A.5 Wave Guide Interpretation

The results of this experiment highlight the effect of reflections and impedance matching, provide experimental evidence for the speed of light being at $2.99 \times 10^8\,m\,s^{-1}$ and show the multiple velocities of electromagnetic waves in transmission lines.

In the first experiment, We can see that the change in impedance from the high to low has the effect of causing reflections in the wave guide and thus causing a delay to our signals. Further it shows that regardless of the delay, or added phase factor, the group velocity of the waves in the wave guide propagate at the speed of light or less.

In the second experiment, we show that the geometry of the wave guide and guide wavelength can be extrapolated with only the knowledge of the frequency of the input signal. Comparing our least squares solution of the wave guide width, we found that $a_{actual} = 2.272\,cm$. Our least squares solutions seems to be incredibly accurate. More interestingly, is that the velocity of the electromagnetic waves we find in the wave guide appear to be faster than the speed of light. This is explained by the fact that we calculated the phase velocity of the waves, which are angled after reflecting off the sides of the wave guide. The wave packet of photons travelling through the wave guide contain an enveloping group velocity travelling at or slower than the speed of light, and plane wave fronts encapsulated. We measure the peaks and troughs of different plane waves angled towards our reader and because of this, the phase velocity appears to be speeding by faster than the speed of light.

A.6 Wave Guide conclusion

Understanding the propagation of waves through our signal chain and the ways in which it is a wave guide are crucial to the understanding of systematic errors that we may find in our results. The phase differences seen in figure 4 are indicative of reflections which could alter the complex components in our results thus effecting our power spectra, temperature calculations and all that follow. Further as we saw in figure 5, the sampling of data from a wave guide may even provide results showing speeds faster than the speed of light, a situation which is clearly not physical and represents a flawed measurement process.

9

B Coordinate Transformations

Here we define the rotation matricies used for coordinate transformations. We first define our coordinates in a spherical system and use galactic coordinates as our starting place.

$$\vec{r}_{galac} = \begin{bmatrix} \cos(b)\cos(l) \\ \cos(b)\sin(l) \\ \sin(b) \end{bmatrix} \tag{17}$$

We then rotate galactic to equitorial using,

$$R_{l,b->\alpha,\delta} = \begin{bmatrix} -0.054876 & 0.494109 & -0.867666 \\ -0.873437 & -0.444830 & -0.198076 \\ -0.483835 & 0.746982 & 0.455984 \end{bmatrix} \tag{18}$$

and the rotation to altitude azimuth as,

$$R_{\alpha,\delta->alt,az} = \begin{bmatrix} -\sin(\phi)\cos(LST) & -\sin\phi\sin(LST) & \cos\phi \\ -\sin(LST) & \cos(LST) & 0 \\ \cos\phi\cos(LST) & \cos\phi\sin(LST) & \sin\phi \end{bmatrix} \tag{19}$$

With this we ca use our vector from equation 17, and multiply to find altitude and azimuth,

$$\vec{r}_{topo} = R_{\alpha,\delta->alt,az}R_{l,b->\alpha,\delta}\vec{r}_{galactic} \tag{20}$$

And finally, with this we can find the altitude and azimuth by extrapolating out the angular positions in the vector so that,

$$alt = \tan^{-1}\left(\frac{r_{topo,y}}{r_{topo,x}}\right)$$
$$az = \sin^{-1}\left(r_{topo,z}\right) \tag{21}$$